Numerical Simulation of Glow Discharges for High-Speed Flow Control

J. Poggie*
Air Force Research Laboratory
Wright-Patterson AFB, OH 45433-7521

N. Sternberg†
Clark University
Worcester, MA 01610

Calculations were carried out with a computer code developed at the Air Force Research Laboratory Computational Sciences Center to model ionized gases with significant charge separation. First, the role of the frictional drag due to ion-neutral collisions in low pressure (~ 0.1 Pa) sheaths was examined. Numerical solutions were compared with experimental data for cathode sheaths with wall potentials of the order 30-100 V. The frictional drag resulting from ion-neutral collisions was represented by a model incorporating both linear and quadratic terms. Good agreement was obtained between the computations and experimental data, and collisional drag was found to have a significant effect on the ion velocity profile and on the overall sheath thickness. The second part of the paper addresses DC glow discharges at relatively high pressure (~ 100 Pa), where ion inertia can be neglected. Preliminary calculations of a nitrogen discharge were carried out, and the solution displayed features in qualitative agreement with standard behavior of DC glow discharges.

Introduction

Over the past few years, the Air Force Research Laboratory Computational Sciences Center has been developing a set of computational tools to study possible electromagnetic flow control techniques.[1–10] A fully three-dimensional magnetohydrodynamic code (`fdl3di-mhd`) suitable for computations at both relatively high and low magnetic Reynolds numbers has been developed.[1,2,4] In addition, a prototype code (`ps3d`) has been written in which the assumption of quasi-neutrality is relaxed in order to examine the plasma sheaths present on electrode surfaces.[6–8] In recent work,[9] this code has been extended to three dimensions and applied to problems with an imposed magnetic field. A newly developed version of the code, described here, introduces the option to model each species either with continuity and momentum equations including inertia, or with a single continuity equation under the drift-diffusion model.

Particle inertia has important effects on the ions in a low-pressure sheath. This physical model is studied in the section "Plasma-Wall Transition," where computations are compared to available experimental data, and the role of the frictional drag due to ion-neutral collisions in low pressure (~ 0.1 Pa) sheaths is examined.

In contrast, ion inertia can be neglected at higher pressures. The work reported in the section "Glow Discharge" exploits this approximation to study DC glow discharges at relatively high pressure (~ 100 Pa).

Plasma-Wall Transition

In this section, the computer code is applied to one-dimensional cathode sheath problems, in the regime where ion inertia is significant. Computational results are compared to available analytical solutions and experimental data, and the influence of the frictional drag due to ion-neutral collisions is examined for the low-pressure (~ 0.1 Pa) regime.

Physical Model

The particle conservation and momentum conservation equations for the ions are:

$$\frac{\partial n_i}{\partial t} + \nabla \cdot (n_i \mathbf{u}_i) = \omega_i \tag{1}$$

$$\frac{\partial}{\partial t}(n_i m_i \mathbf{u}_i) + \nabla \cdot (n_i m_i \mathbf{u}_i \mathbf{u}_i + p_i \mathbf{I}) = q_i n_i \mathbf{E} + \mathbf{F}_i \tag{2}$$

where n_i is the ion number density, $\mathbf{u}_i$ is the ion velocity vector, m_i is the mass per particle, p_i is the ion pressure, and $\mathbf{E} = -\nabla\phi$ is the electric field. The equation of state is:

$$p_i = n_i k_B T_i \tag{3}$$

*Research Aerospace Engineer, AFRL/VAAC. Senior Member AIAA.

†Professor, Department of Mathematics and Computer Science.

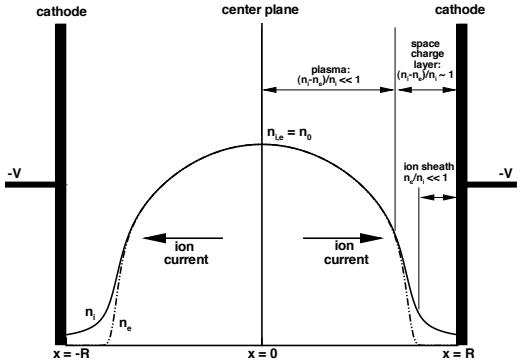

Fig. 1 Diagram of the bounded plasma problem.

where the ion temperature T_i is taken to be constant. We assume singly-ionized atoms: $q_i = +e$. The charged particles are assumed to be produced by 'direct' ionization:

$$\omega_i = z n_e \tag{4}$$

where z is a constant ionization frequency and n_e is the electron number density. The frictional force due to collisions between the ions and the neutral background gas is taken to have the form:[11]

$$\mathbf{F}_i = -\frac{2\sqrt{3}}{\lambda_i}\sqrt{\frac{k_B T_i}{m_i} + \frac{\pi^2 |\mathbf{u}_i|^2}{48}}\, n_i m_i \mathbf{u}_i \tag{5}$$

where λ_i is the ion mean free path.

Equation (5) has two limiting forms, depending on the parameter $\mathcal{M} = |\mathbf{u}_i|/\sqrt{k_B T_i/m_i}$, which is a Mach number based on the ion temperature. The constant ion mobility regime occurs for $\mathcal{M}^2 \ll 48/\pi^2$, which is the typical case for relatively high pressure plasmas. The friction drag becomes $\mathbf{F}_i = -\nu_c\, n_i m_i \mathbf{u}_i$, where $\nu_c = 2\sqrt{3}/\lambda_i \sqrt{k_B T_i/m_i}$ is the ion collision frequency under weak electric fields, and $\mu_i = |q_i|/(m_i \nu_c)$ is the corresponding ion mobility. The ion-charge exchange regime occurs for $\mathcal{M}^2 \gg 48/\pi^2$, which is the typical case for low pressure plasmas. In this case, the friction term becomes $\mathbf{F}_i = -\pi |\mathbf{u}_i|/(2\lambda_i)\, n_i m_i \mathbf{u}_i$.

The electrons are assumed to be in Boltzmann equilibrium with the electric field:

$$n_e = n_0 \exp\left(\frac{e\phi}{k_B T_e}\right) \tag{6}$$

where the electron temperature T_e is assumed to be constant.

The electric potential is determined by the Poisson equation:

$$\nabla^2 \phi = -\zeta/\epsilon_0 \tag{7}$$

where ϵ_0 is the permittivity of free space, and $\zeta = q_i n_i - e n_e$ is the space charge density.

Computations vs. Theory

We consider a problem in which an ionized gas is confined between a pair of electrodes a distance $2R$ apart. The electrodes are assumed to be maintained at a constant negative potential, and to draw an ion current that is maintained by ionization in the plasma.

The configuration is shown in Fig. 1. The problem is symmetric about the plane $x = 0$, where the ion and electron number densities have a maximum value n_0. Because of this symmetry, the ion current is zero at the center plane, but increases farther away, flowing into the walls (cathodes) on either side at $x = \pm R$.

Number density profiles, representative of a collisionless case, are included in the diagram, along with some nomenclature describing various regions in the profiles. The ion and electron number densities, indicated respectively as solid and dash-dot-dot lines, are essentially equal in the perturbed plasma near the center. Closer to the electrodes in the space charge layer, the electron number density falls significantly below the ion number density. Eventually, the electron number density becomes negligible in the ion sheath, which is a subset of the space charge layer.

Theory

Assuming a one-dimensional, steady-state problem, the governing equations (1), (2), (6), and (7) reduce to the following form:

$$\frac{d}{dx}(n_i u_i) = z n_e \tag{8}$$

$$\frac{d}{dx}(m_i n_i u_i^2) + k_B T_i \frac{dn_i}{dx} = -e n_i \frac{d\phi}{dx} - \frac{2\sqrt{3}}{\lambda_i}\left[\frac{k_B T_i}{m_i} + \frac{\pi^2 u_i^2}{48}\right]^{1/2} n_i m_i u_i \tag{9}$$

$$n_e = n_0 \exp\left(\frac{e\phi}{k_B T_e}\right) \tag{10}$$

$$\epsilon_0 \frac{d^2\phi}{dx^2} = -e(n_i - n_e) \tag{11}$$

We assume the following boundary conditions, which represent symmetry about the center plane and an imposed potential at the wall:

$$\begin{array}{ll} n_i(0) = n_0 & u_i(0) = 0 \\ \phi(0) = 0 & \phi'(0) = 0 \\ \phi(R) = \phi_w & \end{array} \tag{12}$$

where $x = 0$ is the plasma center and $x = R$ is the position of the wall (right hand cathode in Fig. 1). For ϕ_w specified, this is a boundary value problem with an eigenvalue z.

We change to the following nondimensional variables, with reference quantities based on the number density at the center plane, the Bohm velocity u_B, and a characteristic potential based on the electron temperature:

$$\begin{array}{ll} \overline{x} = zx/u_B & \eta = -e\phi/(k_B T_e) \\ y = n_i/n_0 & \overline{u} = u_i/u_B \\ y_e = n_e/n_0 & u_B = \sqrt{k_B T_e/m_i} \end{array} \tag{13}$$

Note the sign change on the potential. Dropping the over-bars on x and u, the resulting equations are:

$$(yu)' = y_e \tag{14}$$

$$(yu^2)' + \tau y' = y\eta' - 2\sqrt{3}\frac{\beta}{q_0 x_w}\left[\tau + \frac{\pi^2 u^2}{48}\right]^{1/2} yu \tag{15}$$

$$y_e = \exp(-\eta) \tag{16}$$

$$(q_0 x_w)^2 \eta'' = y - y_e \tag{17}$$

where $\beta = \lambda_{D0}/\lambda_i$, $q_0 = \lambda_{D0}/R$, $x_w = zR/u_B$, $\tau = T_i/T_e$, and $\lambda_{D0} = \sqrt{\epsilon_0 k_B T_e/(n_0 e^2)}$ is the Debye length. The corresponding nondimensional boundary conditions are:

$$\begin{array}{ll} y(0) = 1 & u(0) = 0 \\ \eta(0) = 0 & \eta'(0) = 0 \\ \eta(x_w) = \eta_w & \end{array} \tag{18}$$

As was discussed in conjunction with Eq. (5), the behavior of the friction force due to ion-neutral collisions, the last term in Eq. (15), depends on $\mathcal{M} = u/\sqrt{\tau}$. If $\mathcal{M}^2 \ll 48/\pi^2$, Eq. (15) reduces to a form with linear friction:

$$(yu^2)' + \tau y' = y\eta' - \alpha_1\, yu \tag{19}$$

where $\alpha_1 = 2\beta\sqrt{3\tau}/(q_0 x_w)$. On the other hand if $\mathcal{M}^2 \gg 48/\pi^2$ and $\tau \ll 1$, Eq. (15) reduces to a form with quadratic friction:

$$(yu^2)' = y\eta' \mp \alpha_2\, yu^2 \tag{20}$$

where $\alpha_2 = \pi\beta/(2q_0 x_w)$, and the negative sign is taken for positive velocities.

A plasma solution is available for each of these limiting forms. Self and Ewald[12] found a solution for the quasi-neutral plasma with a linear friction term, Eqs. (14), (16), (17), and (19), with $y = y_e$. Note that only the center ($x = 0$) boundary conditions are satisfied, and the sheath is lost, in the plasma approximation to the full model. The solution is:

$$x = \frac{\sqrt{1+\tau}\,(2+\alpha_1)}{(1+\alpha_1)^{3/2}} \times \arctan\left[\sqrt{\frac{1+\alpha_1}{1+\tau}}\,u\right] - \frac{u}{1+\alpha_1} \tag{21}$$

$$y = \left[1 + \frac{1+\alpha_1}{1+\tau}u^2\right]^{-\frac{2+\alpha_1}{2+2\alpha_1}} \tag{22}$$

$$\eta = -\ln y \tag{23}$$

In the other limit, an analytical plasma solution has been found for quadratic friction (N. Sternberg, unpublished work). This is a solution of Eqs. (14), (16), (17), and (20), with $y = y_e$. It is a generalization of the solution found by Godyak and Maximov,[13] who neglected ion inertia.

The result is:

$$\begin{aligned} x =& B\ln(u-u_0) \\ & - \frac{1+\alpha_2 B}{2\alpha_2}\ln\left(\alpha_2 u^2 - \frac{u}{u_0^2} - \frac{1}{u_0}\right) \\ & - \frac{2\alpha_2 u_0 + 3\alpha_2 B + 1}{\alpha_2\sqrt{3+4u_0^2}}\arctan\left(\frac{2\alpha_2 u_0^2 u - 1}{\sqrt{3+4u_0^2}}\right) \\ & - C \end{aligned} \tag{24}$$

$$\begin{aligned} \eta =& A\ln(u-u_0) \\ & + \frac{1-A}{2}\ln\left(\alpha_2 u^2 - \frac{u}{u_0^2} - \frac{1}{u_0}\right) \\ & + \frac{1-3A}{\sqrt{3+4u_0^2}}\arctan\left(\frac{2\alpha_2 u_0^2 u - 1}{\sqrt{3+4u_0^2}}\right) - K \end{aligned} \tag{25}$$

with

$$y = \exp(-\eta) \tag{26}$$

where

$$A = \frac{1-u_0^2}{3+u_0^2} \tag{27}$$

$$B = \frac{u_0^3 - u_0}{u_0^2 + 3} \tag{28}$$

$$\begin{aligned} C =& \frac{3\alpha_2 B + 1}{2\alpha_2}\ln(-u_0) - \\ & \frac{2\alpha_2 u_0 + 3\alpha_2 B + 1}{\alpha_2\sqrt{3+4u_0^2}}\arctan\left(\frac{-1}{\sqrt{3+4u_0^2}}\right) \end{aligned} \tag{29}$$

$$\begin{aligned} K =& \frac{3A-1}{2}\ln(-u_0) + \\ & \frac{1-3A}{\sqrt{3+4u_0^2}}\arctan\left(\frac{-1}{\sqrt{3+4u_0^2}}\right) \end{aligned} \tag{30}$$

and the parameter u_0 is the root of the polynomial $\alpha_2 u_0^3 + u_0^2 + 1 = 0$.

Results

A set of computations was carried out for the bounded plasma problem using the computer code. The bulk gas (argon) was assumed to be at rest, one species of singly-ionized, positive ions was considered, and the electrons were assumed to be in Boltzmann equilibrium. The computational grid consisted of $101 \times 3 \times 3$ points. The boundary conditions for the calculations were:

$$\begin{array}{ll} n_i(0) = n_0, & \frac{\partial u_i}{\partial x}(0) = z, \\ \phi(0) = 0, & \phi(R) = \phi_w \end{array} \tag{31}$$

The condition on the derivative of the ion velocity at the center is derived from Eq. (8), using $u_i(0) = 0$. This form was more convenient for the numerical calculations, and the ion velocity at the center was observed to converge to zero as time increased.

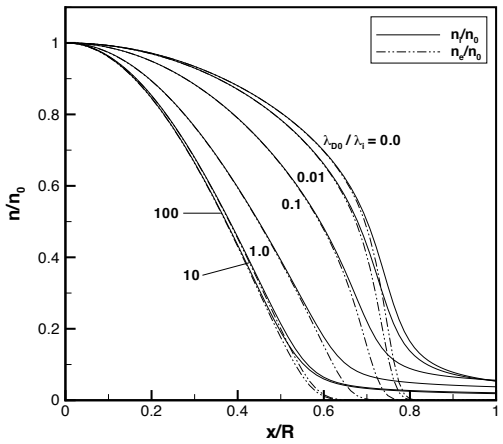

Fig. 2 Number density distribution computed for various collision rates.

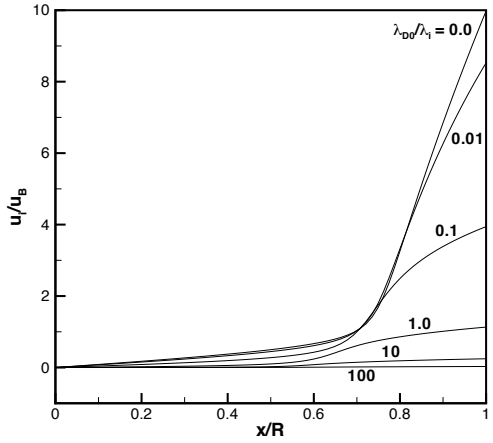

Fig. 3 Ion velocity distribution computed for various collision rates.

An outflow boundary condition, or perfectly absorbing wall, was imposed at the cathode, and other boundary values were found by extrapolation. Uniformity was imposed along the y- and z-directions.

A procedure based on the integral form of the particle conservation equation was used to estimate at each time step in the computations the ionization frequency z required to achieve a steady state. Integrating the continuity equation (8) from the plasma center at $x = 0$ to the electrode at $x = R$, we find:

$$z = \frac{(n_i u_i)_{x=R}}{\int_0^R n_e dx} \tag{32}$$

The calculations were marched in time until the change of the ionization frequency and the independent variables with each time step had reached a minimum.

Figures 2-4 show the profiles of the three dependent variables n_i, u_i, and ϕ for several example calculations. In each case, $q_0 = 0.01$, $\eta_w = 50$, and $\tau = 0.026$. Values of the nondimensional collision parameter are shown from $\beta = 0$ (collisionless) to $\beta = 100$ (highly collisional). A typical set of dimensional conditions corresponding to these values would be $T_i = 300$ K (0.026 eV), $T_e = 11600$ K (1 eV), $\phi_w = -50$ V, $n_0 = 1\times10^{14}$ m^{-3}, and $R = 74$ mm. Under these conditions, the Debye length is $\lambda_{D0} = 0.74$ mm, and the ion mean free path ranges from $\lambda_i = 7.4$ μm to 74 mm for the collisional cases. For argon, $m_i = 6.63 \times 10^{-26}$ kg, and the corresponding Bohm velocity is about $u_B = 1600$ m/s.

Figure 2 shows the number density distributions for the ions and electrons. Near the center ($x/R = 0$), quasi-neutrality prevails, and the number densities of the ions and electrons match closely. Closer to the cathode ($x/R \approx 0.7$ for the collisionless case), the electron number density falls to a value somewhat lower than the ion number density, marking the beginning of the space charge layer. Even closer to the wall ($x/R \approx 0.8$ for the collisionless case), the electron number density becomes completely negligible at the beginning of the ion sheath.

For increasing collision rates (higher values of β), the sheath becomes thicker and the character of the number density distribution changes. The less collisional cases reflect primarily the action of the quadratic term in the friction drag, Eq. (5), and the more collisional cases reflect the linear component.

Figure 3 shows the distribution of the ion velocity for different levels of collisionality. The positive values of ion velocity correspond to ion flow to the right, into the cathode. One point of note is the extremely high velocities that occur near the cathode for low collision levels. For the collisionless case, for example, the ion velocity at the cathode is about 16 km/s. As the collision rate increases, these values drop, and for β greater than about one, the ion velocity is less than the Bohm velocity throughout the solution domain.

Another result of interest is that for low collision values (*e.g.*, $\beta = 0.01$), the velocity distribution nearly coincides with the collisionless case, except in the ion sheath where speeds are reduced by the action of the quadratic friction term. This contrasts with the usual view of a collisional plasma adjacent to a collisionless sheath, a situation that only holds when the wall is near the floating potential.

The corresponding distributions of electric potential are shown in Fig. 4. The major part of the potential drop is seen to occur in the ion sheath. (Compare the length scales with those in Fig. 2.) As also seen in the previous figures, the sheath becomes thicker for higher collision rates.

The relative importance of linear and quadratic friction was examined by comparing numerical solutions of the full model with the analytical plasma solutions for the two limiting cases. The values for the ionization frequency z were taken from the numerical solution of

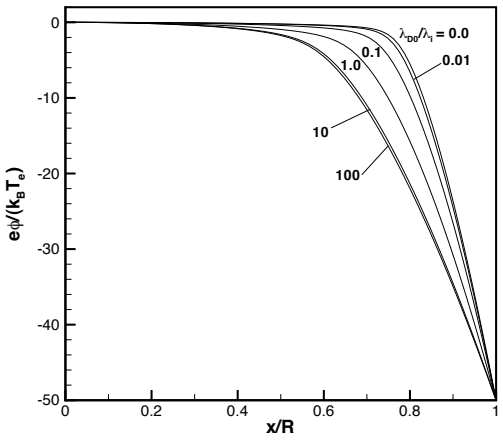

Fig. 4 Distribution of electric potential computed for various collision rates.

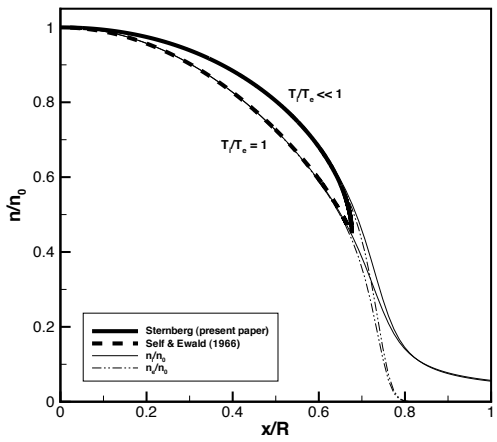

a) Very cold ($\tau = 9 \times 10^{-11}$) and very warm ($\tau = 1$) ions.

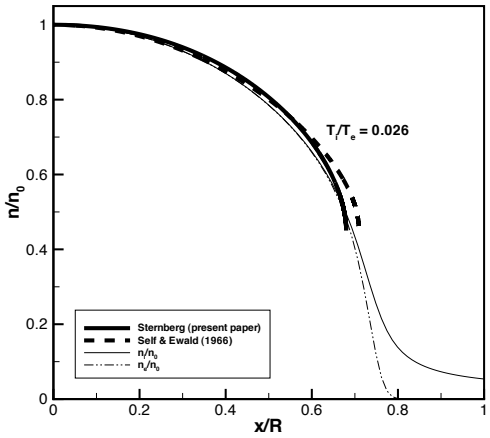

b) Typical case: $\tau = 0.026$.

Fig. 5 Plasma solution versus full model for a slightly collisional case ($\beta = 0.01$), with various ion temperatures.

the full model, and used as inputs to the plasma solutions. The results are presented in Fig. 5, which shows a slightly collisional case ($\beta = 0.01$) for several values of the ion temperature. The other parameters are the same as in Figs. 2-4: $q_0 = 0.01$ and $\eta_w = 50$.

Figure 5a compares the two plasma solutions to numerical computations for cases in which the analytical solutions are good approximations. The Sternberg solution (24)-(30) is seen to agree well with the full model for the cold ion ($\tau \ll 1$) case. The Self-Ewald solution (21)-(23) is seen to agree with the full model for the warm ion ($\tau = 1$) case. The close agreement, in their regime of applicability, between the analytical solutions and the numerical computations indicates the correct implementation of the mathematical model in the computer code.

Figure 5b shows a more typical case: $\tau = 0.026$. Here the Self-Ewald solution agrees well with the full solution near the center, whereas the Sternberg solution has the same shape as the full solution closer in, but is translated up due to its inapplicability near the center. These results suggest that the use of the full frictional drag model, rather than the limiting linear or quadratic forms, may be necessary for accurate modeling of experiments.

Computation vs. Experiment

Here we compare the theory represented by Eqs. (1)-(7), and Eqs. (31)-(32), to two sets of experimental data for low-pressure ($\sim$ 0.1 Pa) argon plasmas. In contrast to the planar symmetry of the theoretical model, which incorporates a pair of cathodes, only one electrode was present in the experiments.

The configuration is shown in Fig. 6. Note that the coordinated system has been changed to correspond to that used in the experimental papers: the cathode is now at $x = 0$.

A steady, one-dimensional solution is not possible

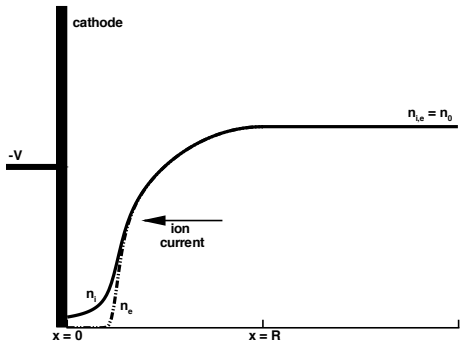

Fig. 6 Schematic diagram of experimental configuration.

Property	Case A	Case B
p	59 mPa	133 mPa
T_e	28000 K	5800 K
T_i	800 K	800 K
n_0	9.8×10^{13} m^{-3}	4.4×10^{14} m^{-3}
ϕ_w	-32.6 V	-32.1 V
λ_i	70 mm	30 mm
λ_{D0}	1.2 mm	0.25 mm

Table 1 Test conditions in the experiments of Oksuz and Hershkowitz.[14]

for a semi-infinite problem with the presence of ionization, so the far-field plasma must be three-dimensional in the experiments. Nevertheless, a one-dimensional model is expected to be applicable in the near-field, and one-dimensional calculations were carried out by selecting an effective half-width R to fit the experimental data.

Oksuz-Hershkowitz Experiments

The first set of experiments considered here was carried out by Oksuz and Hershkowitz[14] in a multi-dipole argon plasma generated by DC-biased hot filaments. The cylindrical test chamber was 350 mm in diameter and 400 mm in height. A 75 mm diameter stainless steel disk was positioned within the uniform portion of the plasma (about 190 mm in diameter and 330 mm high), at a location 100 mm from the sidewalls and 160 mm from the top of the test chamber. The plate was maintained at -30 V with respect to the grounded chamber walls.

The plasma potential was measured using an emissive probe in the limit of zero emission. The probe was traversed along the axis of the disk electrode to obtain the centerline profile of electric potential. Data were obtained at several working pressures; two cases that displayed a wide variation in relative length scales were selected by the present authors for comparison with the computations.

The corresponding experimental conditions are given in Table 1. The wall potential shown in Table 1 is referenced to a value of zero in the bulk plasma. The value is slightly lower than the value of -30 V maintained between the electrode and ground, because the the potential of the bulk plasma was a few volts above that of the grounded chamber walls. The authors report ion temperatures, measured using laser-induced fluorescence, in the range of 500-1200 K (0.04-0.10 eV), with higher values near the electrode and lower values in the bulk plasma. A mid-range value of $T_i = 800$ K was taken for the computations. The nondimensional parameters for Cases A and B are respectively: $\beta = 1.7 \times 10^{-2}$ and 8.4×10^{-3}, $\eta_w = 14$ and 64, $q_0 = 9.3 \times 10^{-3}$ and 2.0×10^{-3}, and $\tau = 0.029$ and 0.14. Note that these are relatively weakly collisional cases, and that the temperature ratio τ is relatively large in Case B.

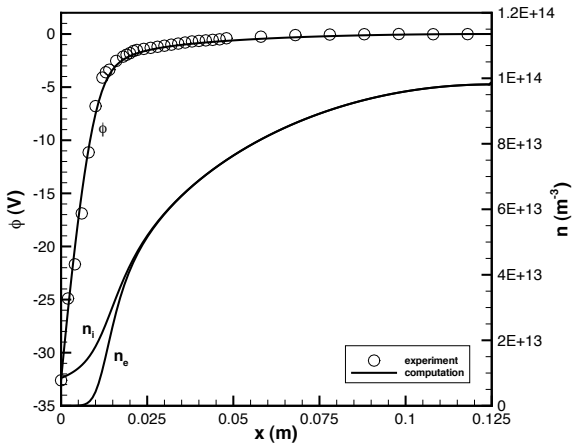

a) Case A.

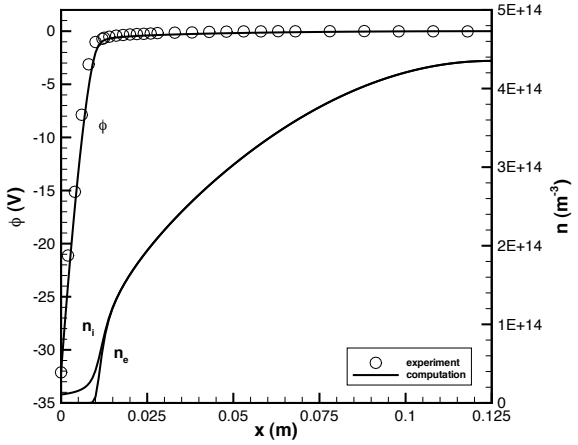

b) Case B.

Fig. 7 Comparison of present computations with experiments of Ref. 14.

Figure 7 compares computational results with experimental data for the plasma potential. As mentioned before, we have now changed coordinate systems so that $x = 0$ at the cathode. The number density distributions for ions and electrons are also shown, in order to illustrate the characteristic widths of the ion sheath and the space charge layer. For both cases, $R = 125$ mm has been taken to fit the experimental data. The agreement between computation and experiment is seen to be excellent in both cases. The thickness of the space charge layer is larger in Case A, corresponding to the larger Debye length in that case.

Figure 8 compares the velocity and potential profiles for the computations shown in Fig. 7 with a

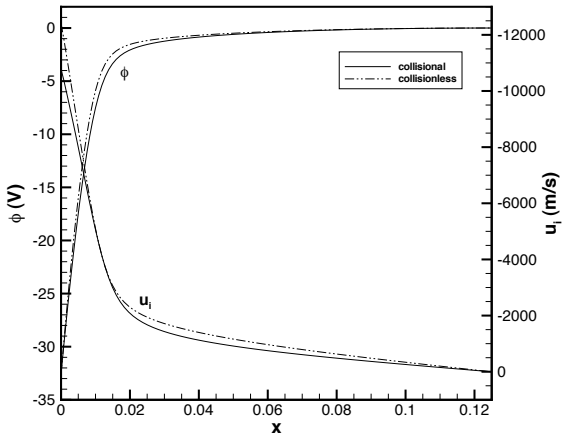

a) Case A.

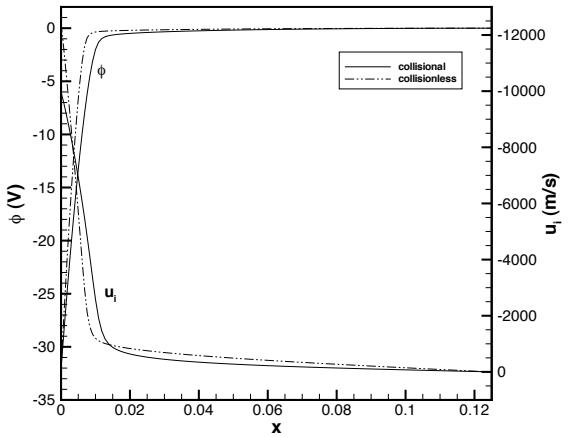

b) Case B.

Fig. 8 Effect of collisions under the conditions of the Oksuz-Hershkowitz experiments.

corresponding set of solutions that neglect the effect of ion-neutral collisions. Despite the relatively large ion mean free path in the baseline collisional cases, $\beta \sim 10^{-3} - 10^{-2}$, collisions are seen to have a significant effect on the profiles of potential and ion velocity. Note also the differences in the shape of the velocity profiles between Case A (small τ) and Case B (relatively large τ).

One of the main points of the Oksuz-Hershkowitz experiments was to examine Riemann's theory of a collisionless sheath and a collisional transition layer.[15] The results presented in Fig. 8 seem to show that collisions can be important in the sheath even for small values of β. The potential is high enough here to accelerate the ions to very high velocities, $\sim 10^4$ m/s, near the cathode, so the quadratic collision term can be quite significant.

Property	Value
p	50 mPa
T_e	6100 K
T_i	300 K
n_0	2.9×10^{14} m^{-3}
ϕ_w	-100.46 V
λ_i	81 mm
λ_{D0}	0.32 mm

Table 2 Test conditions in the experiments of Goeckner, Goree, and Sheridan.[16]

Experiments of Goeckner, Goree, and Sheridan

The second set of experiments considered here were carried out by Goeckner, Goree, and Sheridan.[16] The experimental procedure for generating the plasma was similar to that of Oksuz and Hershkowitz.[14] Again, an argon plasma was generated in a vacuum chamber by primary electrons emitted from a set of DC-biased hot filaments, and confined by a multi-dipole magnetic field. The test chamber was 320 mm in diameter, and the electrode was a 50 mm diameter disk. The electrode was maintained at -100 V with respect to the grounded sidewalls of the test chamber. Relative values of the ion number density and absolute velocities of the ions were measured using laser-induced fluorescence (LIF).

The experimental conditions are listed in Table 2. The authors reported that the ions were at room temperature, based on previous LIF measurements. The parameters in the bulk plasma were measured using a Langmuir probe. The potential there was +0.46 V with respect to the chamber sidewalls, and the electron temperature was 0.53 eV. The ion mean free path was estimated by the present authors to be $\lambda_i = 1/(330\text{cm}^{-1}\text{torr}^{-1}p) = 81$ mm. The corresponding nondimensional parameters are: $\beta = 3.9 \times 10^{-3}$, $\eta_w = 190$, $q_0 = 4.6 \times 10^{-3}$, and $\tau = 0.049$.

Computational results for several different theoretical models are compared to the experimental results in Fig. 9. The effective plasma half-width was taken to be $R = 70$ mm for these computations.

Figure 9a shows the ion number density profile. The experimental measurements are shown along with computations corresponding to the experimental conditions. Goeckner *et al.* compared their experimental results to a collisionless model without ionization. Here three different theoretical curves are shown, corresponding to three different assumptions: a model with ionization and collisional friction, a model with ionization but no collisions, and a model with neither ionization nor collisions. Ionization is seen to play a significant role relatively far from the electrode ($x > 0.025$ m), where the theoretical model without ionization falls substantially below the experimental

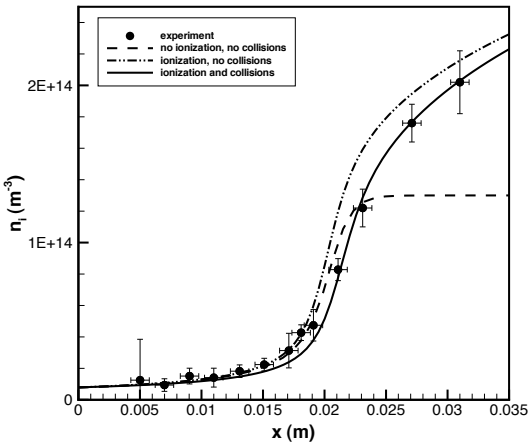

a) Number densities.

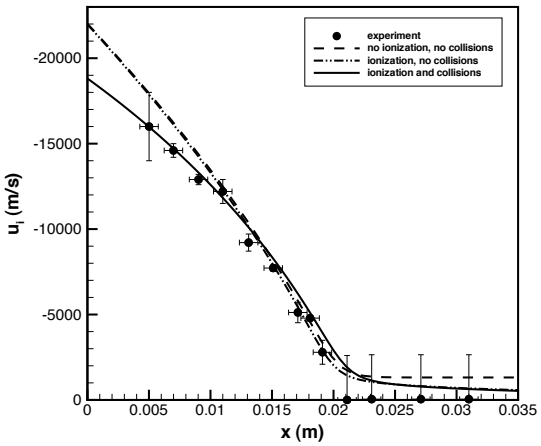

b) Ion velocity.

Fig. 9 Comparison of present computations with experiments of Ref. 16.

data. Elsewhere, the difference between the theories is comparable to the experimental uncertainty, but the model with both ionization and collisions gives the best overall fit.

Figure 9b compares the ion velocities measured by Goeckner *et al.* with the predictions of the three theoretical models. For $x > 10$ mm, all three models are consistent with the experimental data, within the measurement uncertainty. Near the wall ($x < 10$ mm), however, only the collisional theory accurately predicts the velocity measurements. The frictional effect of collisions is seen to have a significant effect on the theoretical prediction, despite the relatively small value of the collision rate β. The reason for this result is that the nonlinear friction term again becomes very large near the cathode due to the squared dependence on velocity.

Glow Discharge

The present section addresses DC glow discharges at relatively higher pressures ($\sim$ 100 Pa), in a regime in which ion inertia can be neglected. Preliminary results for a nitrogen discharge calculation are presented, and the solution features are discussed. Future work will address the quantitative verification and validation of this version of the code.

Physical Model

The conservation of mass, momentum, and energy for the overall gas is expressed as:

$$\frac{\partial \rho}{\partial t} + \nabla \cdot (\rho \mathbf{u}) = 0 \tag{33}$$

$$\frac{\partial}{\partial t}(\rho \mathbf{u}) + \nabla \cdot (\rho \mathbf{u}\mathbf{u} - \boldsymbol{\Sigma}) = \zeta \mathbf{E} + \mathbf{j} \times \mathbf{B} \tag{34}$$

$$\frac{\partial \mathcal{E}}{\partial t} + \nabla \cdot (\mathbf{u}\mathcal{E} - \boldsymbol{\Sigma} \cdot \mathbf{u} + \mathbf{Q}) = \mathbf{E} \cdot \mathbf{j} \tag{35}$$

where the total fluid energy is defined as $\mathcal{E} = \rho(\epsilon + u^2/2)$, and $\epsilon = C_v T$ is the internal energy. The electric and magnetic fields are $\mathbf{E}$ and $\mathbf{B}$, and $\mathbf{u}$ is the fluid velocity. The mass density, the charge density, and the total electric current density are found by summing over all species: $\rho = \Sigma_s m_s n_s$, $\zeta = \Sigma_s q_s n_s$, and $\mathbf{j} = \Sigma_s q_s n_s \mathbf{v}_s$. The total stress tensor $\boldsymbol{\Sigma}$ is given by the usual constitutive equation for a Newtonian fluid and the heat flux $\mathbf{Q}$ follows Fourier's heat conduction law:

$$\Sigma_{ij} = -p\delta_{ij} + \tau_{ij} \tag{36}$$

$$\tau_{ij} = \mu \left(\frac{\partial u_i}{\partial x_j} + \frac{\partial u_j}{\partial x_i} \right) - \frac{2}{3}\mu \frac{\partial u_k}{\partial x_k}\delta_{ij} \tag{37}$$

$$Q_i = -k \frac{\partial T}{\partial x_i} \tag{38}$$

where μ and k are, respectively, the viscosity and thermal conductivity, and the subscripts indicate Cartesian tensor components.

Neglecting acceleration terms and temperature gradients, and defining the diffusion velocity and flux as $\mathbf{w}_s = \mathbf{v}_s - \mathbf{u}$ and $\boldsymbol{\Gamma}_s = n_s \mathbf{w}_s$, respectively, the particle and momentum conservation equations for each species are:

$$\frac{\partial n_s}{\partial t} + \nabla \cdot (n_s \mathbf{u} + \boldsymbol{\Gamma}_s) = \omega_s \tag{39}$$

$$\boldsymbol{\Gamma}_s - s_s \mu_s \boldsymbol{\Gamma}_s \times \mathbf{B} = -D_s \nabla n_s + s_s n_s \mu_s (\mathbf{E} + \mathbf{u} \times \mathbf{B}) \tag{40}$$

where s is the sign of q.

We define the second-order tensor:

$$M^s_{ij} = \frac{1}{1 + \mu_s^2 B^2} \left(\delta_{ij} + \mu_s^2 B_i B_j + s_s \mu_s \epsilon_{ijk} B_k \right) \tag{41}$$

Taking the dot product of $\mathbf{M}^s$ with both side of (40), we find:

$$\boldsymbol{\Gamma}_s = \mathbf{M}^s \cdot [-D_s \nabla n_s + s_s n_s \mu_s (\mathbf{E} + \mathbf{u} \times \mathbf{B})] \tag{42}$$

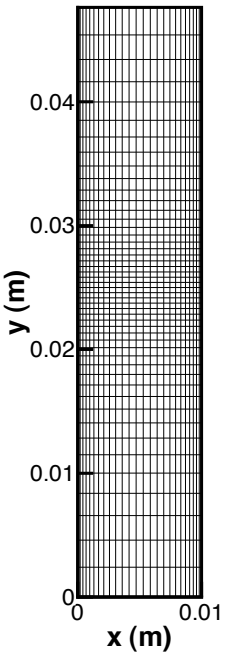

Fig. 10 Computational grid of 101×51 points. Every fourth grid line shown along the x-direction.

where the dot product corresponds to summation on the second index of M^s_{ij}.

Using $\mathbf{E} = -\nabla\phi$, substituting into (39), and rearranging, gives:

$$\frac{\partial n_s}{\partial t} + \nabla \cdot (n_s \mathbf{U}) = \nabla \cdot (D_s \mathbf{M}^s \cdot \nabla n_s) + \omega_s \qquad (43)$$

where $\mathbf{U} = \mathbf{u} + s_s \mu_s \mathbf{M}^s \cdot (-\nabla\phi + \mathbf{u} \times \mathbf{B})$ is the sum of the convection and drift velocities. Equation (43) is the basic drift-diffusion equation.

For the present work, we take the charged particle generation rate to be:

$$\omega_{i,e} = \alpha(E, n)\Gamma_e - \beta n_i n_e \qquad (44)$$

where α is the ionization coefficient, β is the recombination coefficient, E is the magnitude of the electric field, Γ_e is the magnitude of the electron flux, and n is the neutral gas number density.

The electric potential is determined from the Poisson equation:

$$\nabla^2\phi = -\zeta/\epsilon_0 \qquad (45)$$

where ϵ_0 is the permittivity of free space.

Results

As an initial verification and exploration exercise, a set of calculations was carried out for a glow discharge in nitrogen, considering two species: singly-charged ions and electrons. For this initial computation, a very simple geometry was selected: a square domain, 10 mm wide by 50 mm high.

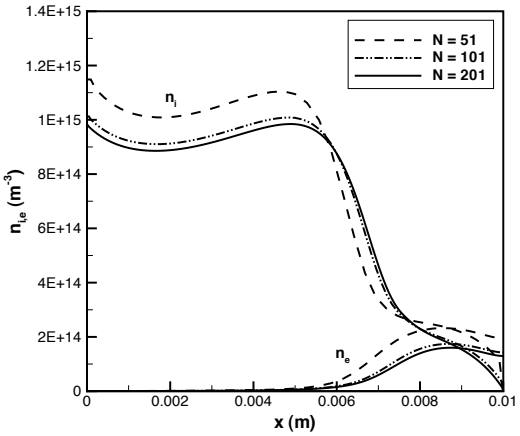

Fig. 11 Grid resolution study of one-dimensional configuration. Conditions: $p = 67$ Pa, $R = 100$ kΩ, $V = 500$ V.

The computational grid of $101 \times 51 \times 3$ points is illustrated in Fig. 10. (Uniformity was imposed in the computation for the three points along the z-direction, and the domain was 10 mm along that direction.) In the figure, the cathode lies on the left at $x = 0$, and the anode lies on the right at $x = 0.01$ m. Points are clustered near the electrode surfaces and also near the centerline. Grid resolution studies of a one-dimensional configuration (Fig. 11) showed that the resolution in the x-direction between the electrodes was adequate. Multi-dimensional grid resolution studies are underway.

The pressure was fixed at 67 Pa everywhere. The electrode temperature was fixed at 300 K, and zero heat flux was specified at the sidewalls. A no-flow condition was imposed over the whole domain, in effect turning off Eqs. (33) and (34), and leaving only heat conduction in Eq. (35). Fluid property data were obtained from Refs. 17 and 18. The electron temperature was assumed to be 11600 K (1 eV).

The ion number density was taken to be zero on the anode, and the electron number density on the cathode was found from the relation:

$$\Gamma_{x,e} = \gamma \Gamma_{x,i} \qquad (46)$$

where $\gamma = 0.1$ is the secondary emission coefficient, and the flux Γ was computed by discretizing Eq. (42) using one-sided, second-order spatial differences. The electron number density at the anode and the ion number density at the cathode were found by extrapolation. On the side boundaries, the number densities of the charged particles were set to zero.

The potential at the anode was taken to be zero, and the normal component of the electric field was set to zero on the side boundaries. The cathode potential V_c was determined according to the circuit shown in Fig. 12. The corresponding ordinary differential equa-

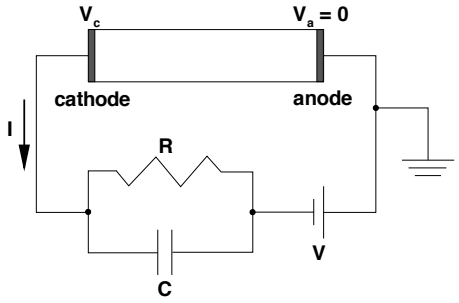

Fig. 12 Circuit diagram of glow discharge.

tion is:

$$RC\,\dot{V}_c + V_c = -V + IR \tag{47}$$

where $V = 500$ V was the applied voltage, $R = 240$ kΩ was the resistance, and I was the total current at the anode predicted by the partial differential equations. The value of the capacitance has no effect on the steady-state solution, and for numerical convenience was taken so that the circuit time constant was $RC = 20\Delta t$, where Δt was the integration time step. Equation (47) was solved using the same discretization as in Eq. (51), and the solution was monitored to determine if it had converged to $V_c = -V + IR$.

Figures 13a-d show profiles of selected quantities along the discharge centerline. The cathode is at the left and the anode is at the right. Number density profiles are shown in Fig. 13a. The cathode sheath is apparent on the left as a region relatively free of electrons, but with a high ion concentration. At right is the anode sheath, which, in contrast to the cathode sheath, is distinguished by a depletion of ions relative to electrons.

A relatively strong electric field is present in the cathode sheath, Fig. 13b, with a weaker field near the anode. Outside the cathode sheath, the current is carried almost entirely by electrons (Fig. 13c). Inside this sheath, the ions make an increasing contribution to the current as the electrode surface is approached.

The corresponding temperature profile is shown in Fig. 13d. The heating is caused by the term $\mathbf{E} \cdot \mathbf{j}$ in Eq. (35). The greatest heating occurs where this term is largest, which is in the cathode sheath. Hence the peak temperature occurs near the sheath edge, with strong heat transfer to the cathode

Figures 14a-d show contour plots of selected quantities in the x-y-plane. The number densities of ions and electrons, Figs. 14a-b, are maximal near the center of the domain, and decline toward the insulator boundaries. The electric potential, Fig. 14c, is relatively uniform along the y-direction. The temperature distribution is shown in Fig. 14d. Again, we see that heat is generated primarily in the vicinity of the cathode sheath, and is conducted away toward the cold electrodes. The strongest temperature gradients and heat transfer occur near the cathode.

The solution is seen to display features in qualitative agreement with standard behavior of DC glow discharges.[19,20] Provisions are included in the code to model the effects of an applied magnetic field, and future work will address this issue, as well as cases with a gas cross-flow.

Discussion

Calculations were carried out with a computer code developed at the Air Force Research Laboratory Computational Sciences Center to model ionized gases with the presence of significant charge separation. Two major options are now available in the code: one to model the motion of each species with continuity and momentum equations, and the other with a single continuity equation under the drift-diffusion model.

First, the role of the frictional drag due to ion-neutral collisions in low pressure (~ 0.1 Pa) sheaths was examined. Numerical solutions were compared with experimental data for weakly-collisional ($\beta \sim 10^{-3} - 10^{-2}$) cathode sheaths with wall potentials of the order $\eta_w \sim 10 - 100$. The frictional drag resulting from ion-neutral collisions was represented by a model incorporating both linear and quadratic terms (constant and variable mobility). For suitable choices of the domain half-width R (see the discussion associated with Fig. 6), good agreement was obtained between the computations and experimental data.

Despite the relatively small values of the nondimensional collision parameter, a significant effect of collisional drag on the ion velocity profile and on the overall sheath thickness was found. In particular, the results contrast with the common view of a collisional plasma adjacent to a collisionless sheath, a situation which only holds when the wall is near the floating potential.

The second part of the paper addressed DC glow discharges at relatively high pressure (~ 100 Pa), where ion inertia can be neglected. Preliminary calculations of a nitrogen discharge were carried out, and the solution displayed features in qualitative agreement with standard behavior of DC glow discharges.

Provisions are included in the code to model the effects of an applied magnetic field, and future work will address this issue, as well as cases with a gas cross-flow.

Appendix: Numerical Methods

The physical models governing the low pressure and high pressure regimes were presented previously in the sections "Plasma-Wall Transition" and "Glow Discharge." The fluid flow equations (33)-(35),

continuity-momentum equations (1)-(2), and the drift-diffusion equation (43) have the common form:

$$\frac{\partial U}{\partial t}+\frac{\partial E}{\partial x}+\frac{\partial F}{\partial y}+\frac{\partial G}{\partial z}=\frac{\partial E_v}{\partial x}+\frac{\partial F_v}{\partial y}+\frac{\partial G_v}{\partial z}+S \quad (48)$$

where U is the solution vector, E, F, and G are convective fluxes, E_v, F_v, and G_v are diffusive fluxes, and S is the source term. We apply the standard transformation from physical coordinates (x, y, z) to grid coordinates (ξ, η, ζ) so that:

$$\frac{\partial \overline{U}}{\partial t}+\frac{\partial \overline{E}}{\partial \xi}+\frac{\partial \overline{F}}{\partial \eta}+\frac{\partial \overline{G}}{\partial \zeta}=\frac{\partial \overline{E}_v}{\partial \xi}+\frac{\partial \overline{F}_v}{\partial \eta}+\frac{\partial \overline{G}_v}{\partial \zeta}+\overline{S} \quad (49)$$

where $\overline{S}=S/J$, $\overline{E}=(\xi_x E+\xi_y F+\xi_z G)/J$, etc.

Equation (49) can be written as:

$$\frac{\partial \overline{U}}{\partial t}=R \quad (50)$$

where R represents the convective fluxes, diffusive fluxes, and source term. Discretizing Eq. (50) in time we write:

$$(1+\theta)\overline{U}^{n+1}-(1+2\theta)\overline{U}^{n}+\theta\overline{U}^{n-1}=\Delta t R^{n+1} \quad (51)$$

where $\theta = 0$ for an implicit Euler scheme and $\theta = 1/2$ for a three point backward scheme. We introduce subiterations such that $\overline{U}^{n+1} \rightarrow \overline{U}^{p+1}$, with $\Delta\overline{U} = \overline{U}^{p+1} - \overline{U}^{p}$. The right hand side R^{n+1} is linearized in the standard 'thin layer' manner.

Collecting the implicit terms on the left hand side, and introducing approximate factoring and a subiteration time step $\Delta\hat{t}$ gives:

$$\mathcal{L}_\xi\mathcal{L}_\eta\mathcal{L}_\zeta\Delta\overline{U}=-\frac{\Delta\hat{t}}{1+\theta}\mathcal{R} \quad (52)$$

where $\mathcal{L}_\xi$, $\mathcal{L}_\eta$, and $\mathcal{L}_\zeta$ are implicit spatial difference operators. For example:

$$\mathcal{L}_\xi=1-\frac{\Delta\hat{t}}{1+\theta}(B+\delta_\xi A+\delta_\xi R\delta_\xi+D_{i\xi}) \quad (53)$$

where B is the source Jacobian, A and R are combinations of the flux Jacobians, and $D_{i\xi}$ represents an optional implicit damping operator. The term $\mathcal{R}$ contains the explicit discretized form of the governing equations:

$$\mathcal{R}=\frac{(1+\theta)\overline{U}^{p}-(1+2\theta)\overline{U}^{n}+\theta\overline{U}^{n-1}}{\Delta t}-R^{p}-D_e\overline{U}^{p} \quad (54)$$

where D_e is an optional explicit damping operator.

For the fluid and low-pressure sheath equations, the spatial derivatives were evaluated using second order central differences. For these cases, the symbols D_i and D_e represent, respectively, variants of the implicit and explicit damping operators described by Pulliam.[21] The explicit damping operator uses a nonlinear blend of second- and fourth-order damping.[22]

For the drift-diffusion equations, the spatial derivatives were evaluated using a second order upwind method based on the drift velocity, employing the MUSCL approach.[23] The minmod limiter was used, and damping was not applied.

Each factor in Eq. (52) was solved in turn using a standard block tridiagonal solver, and $\Delta\overline{U}$ was driven to zero by the subiteration procedure. The Poisson equation, species equations, and the fluid equations were solved inside this subiteration loop in a loosely-coupled fashion.

The Poisson equation was solved using an approximately factored implicit scheme, adapted from the approach described by Holst.[24] The three-dimensional Poisson equation (7) can be written in the form:

$$\frac{\partial E}{\partial x}+\frac{\partial F}{\partial y}+\frac{\partial G}{\partial z}=S \quad (55)$$

where $E = \partial\phi/\partial x$, $F = \partial\phi/\partial y$, $G = \partial\phi/\partial z$, and $S = -\zeta/\epsilon_0$. Applying the standard transformation of coordinates, this becomes:

$$\frac{\partial \overline{E}}{\partial \xi}+\frac{\partial \overline{F}}{\partial \eta}+\frac{\partial \overline{G}}{\partial \zeta}=\overline{S} \quad (56)$$

where $\overline{S}=S/J$, $\overline{E}=(\xi_x E+\xi_y F+\xi_z G)/J$, etc.

Following the procedure described by Holst, we introduce an artificial time term:

$$\frac{\partial\phi}{\partial\tau}=L\phi=\frac{\partial \overline{E}}{\partial \xi}+\frac{\partial \overline{F}}{\partial \eta}+\frac{\partial \overline{G}}{\partial \zeta}-\overline{S} \quad (57)$$

and develop a procedure that drives the numerical solution towards $L\phi = 0$.

We write $\Delta\phi/\Delta\tau = L\phi^{p+1}$, where $\Delta\phi = \phi^{p+1} - \phi^{p}$, then linearize the right hand side using the standard 'thin layer' approach. We also introduce $\alpha = 1/\Delta\tau$, an over-relaxation parameter ω, and approximate factoring:

$$\mathcal{L}_\xi\mathcal{L}_\eta\mathcal{L}_\zeta\Delta\phi=\omega\alpha^{-1}L\phi^{p} \quad (58)$$

where, for example, the ξ-operator is:

$$\mathcal{L}_\xi=1+\alpha^{-1}(D-\delta_\xi A\delta_\xi) \quad (59)$$

and D and A are, respectively, the source and flux Jacobians.

The spatial derivatives were evaluated using a central difference approach, and the resulting tridiagonal system for each factor was solved using the Thomas algorithm.

In order to accelerate convergence, the pseudo-time parameter was varied according to the procedure:

$$\alpha_p=\alpha_H\left(\frac{\alpha_L}{\alpha_H}\right)^{\frac{p-1}{M-1}} \quad (60)$$

where α_L and α_H are the low and high bounds on α_p, and p cycles periodically between 1 and M.

Acknowledgments

This project was sponsored in part by grants from the Air Force Office of Scientific Research (monitored by W. Hilbun, J. Schmisseur, F. Fahroo, and A. Nachman), and by grants of High Performance Computing time from the Department of Defense Major Shared Resource Centers at the Naval Oceanographic Office (NAVO), the Arctic Region Supercomputing Center (ARSC), and the Aeronautical Systems Center (ASC). The first author would like to acknowledge the help of a number of his colleagues at AFRL/VAAC in developing the computer code, including D. Gaitonde, D. Rizzetta, and M. White. We would also like to thank I. Adamovich, M. Shneider, and V. Godyak for helpful comments and suggestions.

References

[1]Gaitonde, D. V., "Higher-Order Solution Procedure for Three-Dimensional Nonideal Magnetogasdynamics," *AIAA Journal*, Vol. 39, No. 1, 2001, pp. 2111–2120.

[2]Poggie, J. and Gaitonde, D. V., "Magnetic Control of Flow Past a Blunt Body: Numerical Validation and Exploration," *Physics of Fluids*, Vol. 14, No. 5, 2002, pp. 1720–1731.

[3]Godyak, V. and Sternberg, N., "On the Consistency of the Collisionless Sheath Model," *Physics of Plasmas*, Vol. 9, No. 11, 2002, pp. 4427–4430.

[4]Gaitonde, D. V. and Poggie, J., "Implicit Technique for Three-Dimensional Turbulent Magnetoaerodynamics," *AIAA Journal*, Vol. 41, No. 11, 2003, pp. 2179–2191.

[5]Poggie, J., "Modeling the Propagation of a Shock Wave through a Glow Discharge," *AIAA Journal*, Vol. 38, No. 8, August 2000, pp. 1411–1418.

[6]Poggie, J. and Gaitonde, D. V., "Electrode Boundary Conditions in Magnetogasdynamic Flow Control," AIAA Paper 2002-0199, January 2002.

[7]Poggie, J., Gaitonde, D. V., and Sternberg, N., "Numerical Simulation of Plasma Sheaths in Aerodynamic Applications," AIAA Paper 2002-2166, May 2002.

[8]Poggie, J., "Numerical Simulation of Electromagnetic Flow Control for Hypersonic Systems," AIAA Paper 2002-5182, October 2002.

[9]Poggie, J. and Sternberg, N., "Numerical Simulation of Electrode Sheaths in a Magnetized Plasma," AIAA Paper 2003-0359, January 2003.

[10]Roy, S., Pandey, B. P., Poggie, J., and Gaitonde, D. V., "Modeling Low Pressure Collisional Plasma Sheath with Space-Charge Effect," *Physics of Plasmas*, Vol. 10, No. 6, 2003, pp. 2578–2585.

[11]Godyak, V. A. and Sternberg, N., "Smooth Plasm-Sheath Transition in a Hydrodynamic Model," *IEEE Transactions on Plasma Science*, Vol. 18, No. 1, 1990, pp. 159–168.

[12]Self, S. A. and Ewald, H. N., "Static Theory of a Discharge Column at Intermediate Pressures," *The Physics of Fluids*, Vol. 9, No. 12, 1966, pp. 2486–2492.

[13]Godyak, V. A. and Maximov, V. N., "On the Space Distribution of a Bounded Plasma," *Vestnik Moskovskogo Universiteta, ser. Fiz. Astr.*, Vol. 18, No. 6, 1977, pp. 51–56, In Russian.

[14]Oksuz, L. and Hershkowitz, N., "First Experimental Measurements of the Plasma Potential throughout the Presheath and Sheath at a Boundary in a Weakly Collisional Plasma," *Physical Review Letters*, Vol. 89, No. 14, 2002, pp. 145001–1–145001–3.

[15]Riemann, K.-U., "The Influence of Collisions on the Plasma Sheath Transition," *Physics of Plasmas*, Vol. 4, No. 11, 1997, pp. 4158–4166.

[16]Goeckner, M. J., Goree, J., and Sheridan, T. E., "Measurements of Ion Velocity and Density in the Plasma Sheath," *Physics of Fluids*, Vol. 4, No. 6, 1992, pp. 1663–1670.

[17]Surzhikov, S. T. and Shang, J. S., "Glow Discharge in Magnetic Field," AIAA Paper 2003-1054, January 2003.

[18]White, F. M., *Viscous Fluid Flow*, McGraw-Hill, New York, 2nd ed., 1991.

[19]Boeuf, J.-P., "A Two-Dimensional Model of DC Glow Discharges," *Journal of Applied Physics*, Vol. 63, No. 5, 1988, pp. 1342–1349.

[20]Raizer, Y. P. and Surzhikov, S. T., "Two-Dimensional Structure in a Normal Glow Discharge and Diffusion Effects in Cathode and Anode Spot Formation," *High Temperature*, Vol. 26, No. 3, 1988, pp. 304–311.

[21]Pulliam, T. H., "Implicit Finite-Difference Simulations of Three-Dimensional Compressible Flow," *AIAA Journal*, Vol. 18, No. 2, 1980, pp. 159–167.

[22]Jameson, A., Schmidt, W., and Turkel, E., "Numerical Solutions of the Euler Equations by a Finite Volume Method Using Runge-Kutta Time Stepping Schemes," AIAA Paper 81-1259, June 1981.

[23]Anderson, W. K., Thomas, J. L., and van Leer, B., "A Comparison of Finite Volume Flux Vector Splittings for the Euler Equations," AIAA Paper 85-0122, January 1985.

[24]Holst, T. L., "Transonic Flow Computations Using Nonlinear Potential Methods," *Progress in Aerospace Sciences*, Vol. 36, 2000, pp. 1–61.

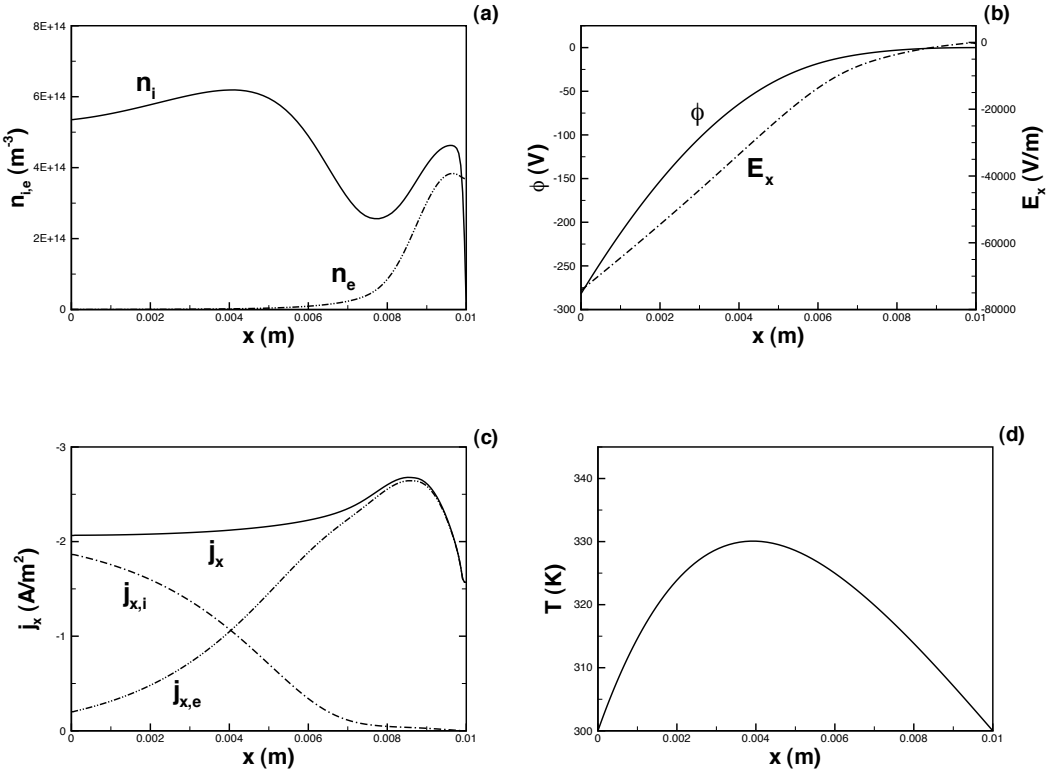

Fig. 13 Profiles along the discharge centerline. (a) Number density. (b) Potential and x-component of electric field. (c) Total, ion, and electron current. (d) Temperature.

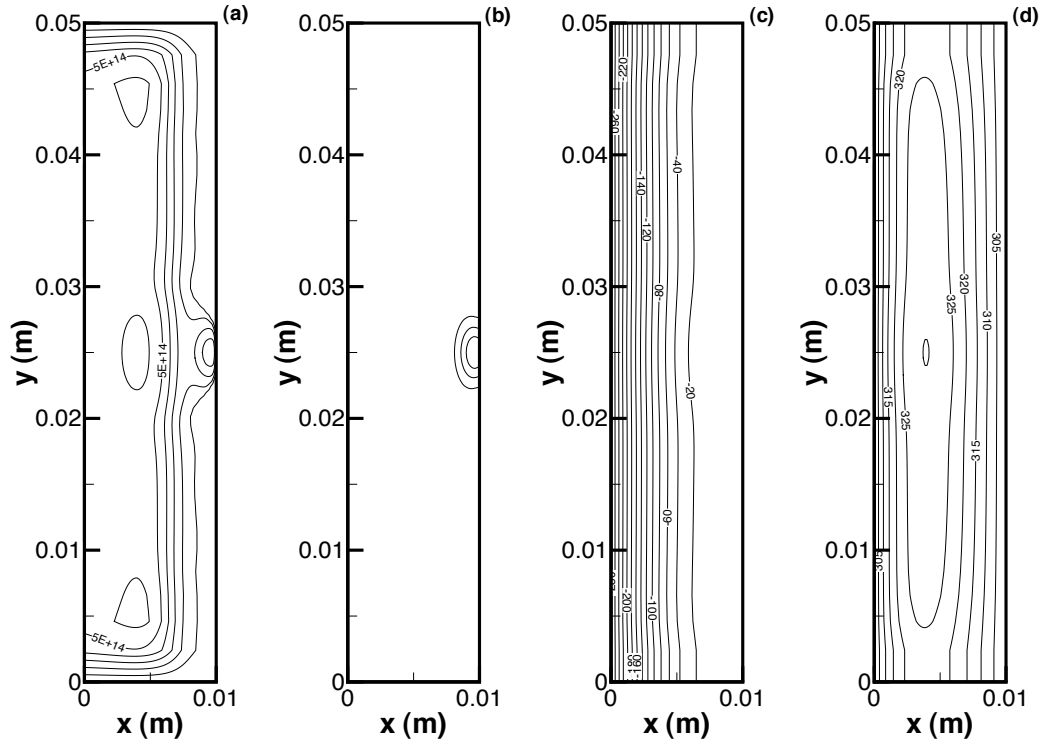

Fig. 14 Contour plots of two-dimensional solution. (a) Ion number density, contour interval 1×10^{14} m^{-3}. (b) Electron number density, contour interval 1×10^{14} m^{-3}. (c) Electric potential (V). (d) Temperature (K).